Experimental Thermal and Fluid Science 177 (2026) 111797

Contents lists available at ScienceDirect

Experimental Thermal and Fluid Science

journal homepage: www.elsevier.com/locate/etfs

Spatially resolved heat transfer measurements of impinging jets on statistically rough surfaces using an infrared-based gradient sensor

Thomas Häber [a,*], Sebastian Moosmayer [c], Francesco Secchi [b], Marco Raiola [e,b], Davide Gatti [b], Dimosthenis Trimis [c], Rainer Suntz [d], Bettina Frohnapfel [b]

[a] *Institute of Catalysis Research and Technology (IKFT), Karlsruhe Institute of Technology (KIT), Hermann-von-Helmholtz-Platz 1, Eggenstein-Leopoldshafen, 76344, Germany*
[b] *Institute of Fluid Mechanics (ISTM), Karlsruhe Institute of Technology (KIT), Kaiserstraße 10, Karlsruhe, 76131, Germany*
[c] *Engler-Bunte-Institut Combustion Technology (EBI-CT), Karlsruhe Institute of Technology (KIT), Engler-Bunte-Ring 7, Karlsruhe, 76131, Germany*
[d] *Institute for Chemical Technology and Polymer Chemistry (ITCP), Karlsruhe Institute of Technology (KIT), Engesserstraße 20, Karlsruhe, 76131, Germany*
[e] *Department of Aerospace Engineering, Universidad Carlos III de Madrid (UC3M), Av. Universidad, 30, Leganés, 28911, Spain*

ARTICLE INFO

Keywords:
Turbulent impinging jet
Infrared thermography
Gradient heat-flux sensor
Surface roughness
Nusselt number distribution

ABSTRACT

Heat-transfer measurements of jets impinging on rough surfaces are scarce because conventional heated-thin-foil methods confine high-resolution measurements to smooth walls. This study presents an infrared-thermography-based gradient sensor that enables spatially resolved wall-heat-flux measurements on thermally thick plates with embedded, statistically homogeneous roughness. The method is validated against direct numerical simulation and established smooth-wall datasets for Reynolds numbers in the range $5000 \leq Re \leq 30\,000$ and nozzle-to-plate distances in the range $2 \leq H/D \leq 5$, showing good accuracy and repeatability. Using two roughness scales ($k_{99}/D = 0.04$ and 0.12), we provide the first systematic dataset of local Nusselt-number distributions for turbulent impinging jets on rough surfaces at Reynolds numbers relevant for practical applications. Roughness is shown to have little effect at low Re, but a pronounced heat-transfer enhancement appears once a combined threshold in roughness height and Reynolds number is exceeded. For the larger roughness, strong augmentation is already observed for $Re \geq 10\,000$, especially near $r/D \approx 1$ where wall-jet shear is highest. At higher Reynolds numbers, roughness appears to fundamentally modify the radial heat-transfer pattern: the secondary peak, typically observed for smooth-wall impingement, disappears, giving way to a bell-shaped Nusselt profile, likely governed by altered near-wall flow dynamics. These findings offer new insight into heat transfer of rough-wall jet impingement at high Re and establish a validated measurement technique suitable for future studies integrating heat transfer, flow-field diagnostics, and wall-shear measurements.

1. Introduction

Impinging jets offer a practical strategy to remove heat from a surface, finding application in numerous industrial processes where effective cooling is required. The wall-normal directed flow typically generates steep temperature gradients at the wall, which, in turn, translate into high heat transfer rates at the target surface. Due to its relevance, heat transfer of impinging-jets has been widely investigated over the years: the present state of knowledge for the heat transfer realized by the impingement of a single circular jet on a smooth plate is nicely summarized in the reviews by Carlomagno and Ianiro [1] and Uddin et al. [2]. A discussion of the related thermal efficiency, i.e. the mechanical power required to drive the flow per unit of heat transfer rate, can be found in [3]. The heat transfer properties are known to depend on the inflow conditions of the jet and the nozzle-to-plate distance. For specific configurations (in which the jet inflow condition corresponds to a fully developed pipe flow), heat transfer is largest in the stagnation point while a secondary local peak in the mean wall-heat flux distribution is observed at a distance of approximately two nozzle diameters from the jet axis [4]. According to the literature on the topic, the occurrence of this secondary peak is linked to Kelvin–Helmholtz instabilities occurring in the shear layers of the free and wall jets. Such instabilities govern the emergence of large-scale toroidal structures which, upon advecting toward the wall, promote the development of smaller-scale vortical structures in the near-wall region [4]. The relation between the instantaneous heat and momentum transfer induced by these structures has been recently investigated by Raiola

* Corresponding author.
E-mail address: thomas.haeber@kit.edu (T. Häber).

https://doi.org/10.1016/j.expthermflusci.2026.111797
Received 27 February 2026; Received in revised form 18 May 2026; Accepted 15 June 2026
Available online 18 June 2026

et al. [5] through a data-driven analysis, suggesting the existence of a similarity between radially traveling waves of these quantities apart from phase delays.

An important aspect which has not been deeply investigated, and capable of affecting the heat transfer of impinging jets, is the presence of surface roughness on the impingement plate. Fundamental research on canonical wall-bounded turbulent flows have demonstrated that surface roughness with a characteristic scale comparable to the viscous length scale can induce substantial drag penalties and enhance mean heat transfer rates relative to flows over hydraulically smooth surfaces [6,7]. In the literature dedicated to impinging jets, studies addressing the effects of surface roughness remain relatively scarce. A recent review by Ekkad and Singh [8] synthesizes much of the available research on this topic. Most of the reported studies restrict the analysis to assessing the overall roughness-related increase in wall-heat transfer for specific setups, including arrays of multiple jets and engineered rough surfaces (e.g., plates with dimples or fins). Regularly spaced fins of various geometries have been reported to enhance the plate-averaged Nusselt number by up to 28% [9,10]. In contrast, Ekkad and Kontrovitz [11], who examined the influence of dimples in a multi-jet configuration, found a reduction in the average Nusselt number compared to a smooth, unstructured wall. Fewer investigations have examined the canonical case of a single circular turbulent jet impinging on a plate with homogeneous random surface roughness [12–15]. Among these, only Secchi et al. [15] address the effects of surface roughness on wall-heat transfer. In all reported studies, the investigated surface roughness only marginally affects the mean flow field. For instance, Secchi et al. [14] shows that the surface roughness causes a minor departure from the self-similarity of the mean velocity profiles along the wall-jet region of the flow. The minor impact of the roughness, however, was attributed to the relatively low Reynolds number $Re = 10\,000$, based on the mean bulk velocity of the jet and nozzle diameter. Furthermore, Secchi et al. [15] report that, for similar rough surfaces and a lower Reynolds number, $Re = 5300$, the mean wall-heat flux distribution along the impingement plate is not significantly affected by roughness.

It is reasonable to link such marginal effects of surface roughness to two key properties. First, the large-scale toroidal structures discussed above are known to play a major role in determining wall-heat transfer phenomena at the impingement plate. Those appear to be scarcely affected by a roughened surface, whose characteristic size is greatly separated from the characteristic size of the toroidal structures (which is typically in the order of the jet nozzle diameter). Second, for turbulence driven by wall shear, the characteristic roughness scale needs to be compared to the characteristic scale of the near-wall turbulence and must exceed it by at least a factor of five for the flow to depart from the hydrodynamically smooth flow regime [16]. While this threshold refers to the impact of roughness on flow resistance (and hence momentum transfer), it is expected to hold in a similar manner for heat transfer. The relevant turbulence scale, in this case, is the classical viscous length scale $\delta_\nu = \nu\sqrt{\rho/\tau_w}$, where ρ and ν are fluid density and kinematic viscosity while τ_w corresponds to the effective wall shear stress. In turbulent flows over smooth walls, τ_w arises exclusively from viscous friction and is thus set by the fluid viscosity and the wall-normal gradient of the mean flow. In rough-wall flows, however, the effective wall shear stress represents the combined effect of friction and pressure drag on the individual roughness elements.

In the jet impingement region τ_w is always small close to the stagnation point. Further outward along the impingement plate a wall-jet develops which induces a wall shear stress distribution that decreases in radial direction [17]. Due to the complexity of the flow field in an impinging jet it is not obvious how τ_w changes with Re. Whether the low sensitivity of jet-impingement heat transfer on surface roughness observed at low Reynolds numbers also applies at higher Reynolds numbers remains unclear. To the authors' knowledge, heat transfer data for turbulent jets impinging on rough surfaces at higher Reynolds number are rare in the literature. This gap in the literature can be attributed both, to the difficulty of achieving high Reynolds numbers in DNS because of the associated computational cost, and to the challenges involved in obtaining reliable heat-transfer measurements over rough surfaces. Consequently, it remains difficult to determine whether surface roughness influences heat transfer in high-Reynolds-number impinging jet flows, particularly in conditions where the roughness dimensions are comparable to or exceed the near-wall thermal and viscous length scales, and the resulting modifications to local heat-transfer behavior are therefore still not well understood.

The heat transfer of a turbulent jet impinging on a smooth plate has been extensively studied through experiments over the past several decades, covering a wide range of nozzle exit Reynolds numbers (Re) and nozzle-to-plate distances (H/D). Table 1 provides a concise summary of prior research exploring the same range of Reynolds numbers addressed in this study. All of those studies employ a heated thin-foil sensor, either through gold or stainless steel films or printed copper circuits, with typical thicknesses of a few tens of micrometers. In terms of detection methods, they can be broadly classified into two groups: liquid crystal [18–22] and infrared imaging techniques [23–29]. In instances where liquid crystals are used, they are typically chosen with a very narrow temperature range of their transition region to ensure a temperature resolution of 0.1 K or better. The entire field of the Nusselt number distribution is examined by gradually changing the Joule heat flux. The color gradient of the liquid crystals is visually inspected [18,19] or digitized by a CCD camera [20–22]. However, most recent studies use an infrared camera (IR) to directly record the two-dimensional (2D) temperature distribution over the impingement surface. The use of the heated-thin-foil sensor limits the practical application of these measurement techniques to smooth-wall cases only, since the heat sensor itself is made of a thin metallic foil on which it is evident that roughness cannot be embedded. To the best of our knowledge, there are no experimental studies that measure spatially resolved, local wall heat-flux or Nusselt-number distributions of turbulent impinging jets on rough surfaces. Existing experiments utilize global heat balances and thermocouples embedded in the surface to provide surface averaged Nusselt numbers [30–32]. As illustrated by Abu Rowin et al. [33], there is a lack of local heat-flux measurement methods on rough walls.

In this study, we perform infrared thermography–based measurements on a thermally thick slab with embedded surface roughness. Using such an approach on a rough surface for the first time, we present experimental measurements of the mean wall heat-flux distributions along both smooth and rough impingement plates for circular jets at various nozzle-to-plate spacings. At the nozzle outlet, we use a fully-developed turbulent pipe flow at different Reynolds numbers to facilitate the reproducibility of the experimental conditions. The surface roughness on the impingement plate is statistically homogeneous in plate parallel directions and was designed to mimic a realistic roughened surface.

2. Experimental set-up

The configuration of the present experimental investigations is an axially symmetric impinging jet which is an extension of the experimental setup presented in Secchi et al. [13] and Bopp et al. [34]. Fig. 1 shows an overview of the nozzle and impingement plate configuration used for the experiment. Following literature, the coordinate origin is located at the impingement point, with the z-axis pointing away from the wall in the direction of the nozzle exit. The jet exits from a pipe of length $\mathrm{L} = 1300\,\mathrm{mm}$ (at ambient pressure and at a temperature of 293 K) in which fully developed flow conditions are reached [34]. The Reynolds number Re is based on the bulk velocity U_b of this pipe flow and the corresponding pipe diameter $D = (25 \pm 0.25)\,\mathrm{mm}$, such that $\mathrm{Re} = U_\mathrm{b} D/\nu$. The influence of different Reynolds numbers in the range $Re = 5000 \ldots 30\,000$ on the wall-heat flux are investigated by varying

Table 1
Heat transfer measurements of circular turbulent impinging jets — a summary of previous literature studies.

Author	Notes	Re	H/D	Ref.
Baughn & Shimizu (1989)	Liquid crystal, heated gold film, visual (colored) rings of isotherms	23 750	2, 6, 10, 14	[18]
Baughn et al. (1991)	Liquid crystal, heated gold film, visual (colored) rings of isotherms	23 300	2, 6, 10	[19]
Lee et al. (1995)	Liquid crystal, heated, gold coated INTREX foil, CCD camera (backside)	4000…14 000	2, 4, 6, 10	[20]
Lee & Lee (1999)	Liquid crystal, heated gold-coated film, CCD camera (backside)	5000…30 000	2, 4, 6, 10	[21]
Lee et al. (2002)	Liquid crystal, heated gold film, video camera (frontside)	23 000	2, 4, 6, 8, 10	[22]
Gao et al. (2003)	Heated stainless steel foil, IR camera (backside)	23 000	2, 4, 6	[23]
Fenot et al. (2005)	Heated copper circuit, IR camera (backside)	23 000	2, 5	[24]
Katti & Prabhu (2008)	Heated stainless-steel foil, IR camera (backside)	12 000…28 000	0.5…8	[25]
Vinze et al. (2016)	Heated stainless steel foil, IR camera (backside)	10 000, 15 000, 23 000	1, 2, 6, 8	[26]
Trinh et al. (2016)	Heated copper circuit foil, IR camera (backside)	23 000	1, 2, 3, 5	[27]
Du et al. (2018)	Heated stainless steel foil, IR camera (backside), conical shaped nozzle, tangential conduction correction (found to be small)	20 000	2, 4, 6	[28]
Yogi et al. (2020)	Heated stainless steel foil, IR camera (backside)	10 000…25 000	2, 4, 6, 8	[29]

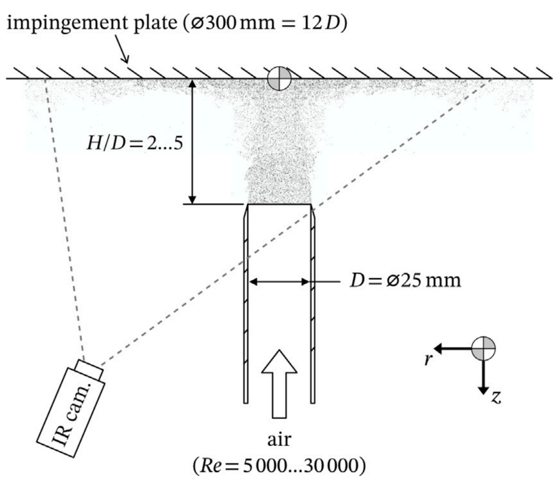

Fig. 1. Schematic overview of the experimental setup for the thermography measurements, using an IR camera to capture the two-dimensional distribution of the wall surface temperature.

Table 2
Summary of test conditions.

Parameter	Symbol	Value
Fluid temperature	T_{jet}	293 K
Wall temperature		330 K
Reynolds number	Re	5000, 10 000, 15 000, 20 000, 25 000, 30 000
Nozzle diameter	D	25 mm
Nozzle/wall distance	H/D	2, 3, 4, 5
Roughness height	k_{99}/D	0.04, 0.12

the volumetric flow rate through the pipe and therefore U_b. A thermal-mass flow controller (Bronkhorst F-203AV or MKS G250 A) is used to control the flow rate.

The impingement plate is located at a distance H from the nozzle outlet, varying between $H/D = 2$ and 5. Three different impingement plates were considered in this study: a smooth impingement plate, which sets the reference condition, and two plates with different surface roughness properties. All impingement plates have a diameter of $12D$ (= 300 mm) and are made of aluminum. The smooth surface is milled with a remaining roughness of $R_a < 3\,\mu$m, where R_a denotes the average absolute deviation of the surface height from the mean surface height. Both rough surfaces have been generated according to a prescribed statistical wall-height distribution (and thus no fixed geometric pattern like the one used e.g. in [10]) to provide a small and large roughness with similar statistical properties. The mean height of the roughness is identical to the location of the smooth reference surface such that roughness peaks are located above this reference level and roughness troughs are located below. The roughness height follows a Gaussian distribution with an effective slope parameter (ES) (as defined in [35]) of $ES = 0.4$. A characteristic roughness length scale can be assigned through k_{99} which encompasses 99% of the surface heights. It measures the wall-normal distance from the lowest roughness trough to the highest roughness peak within this range. For the small roughness it holds that $k_{99} = 0.04\,D = 1$ mm. The large roughness is three times larger, resulting in $k_{99} = 0.12\,D = 3$ mm. Details of the surface design and the production of the rough surfaces are reported in [13] with further reference to Pèrez-Ràfols and Almqvist [36] and Forooghi et al. [37]. The flow properties of the impinging jet for the two different rough surfaces and the smooth wall reference plate at low Reynolds numbers can be found in previous publications [13,34].

The local heat flux over the impingement plate is measured over a circular region with a radius of $4D$ as described in the following section. Results are presented as functions of the radial coordinate r, based on data averaged in time and in circumferential direction. Table 2 provides a comprehensive overview of the experimental conditions and the corresponding ranges of the parameters varied in this study.

3. Heat flux measurement

In the present work, Nusselt number distributions are estimated indirectly by measuring wall surface temperatures and a simple heat transfer model using a so-called *gradient sensor* [38,39]. The sensor comprises a thermally-thick wall: from the knowledge of the temperature difference across the slab (wall), it allows to solve for the convective heat transfer on the side interested by the jet impingement from the heat balance equation. The temperature of the back surface is conditioned with circulating thermal oil (Aral Farolin U) at a prescribed temperature. Thermal conditioning is achieved by two intertwined spiral channels for thermal oil on the back of the wall, its temperature being controlled by a thermostat (Single Compact Oil DM-250) between 300 and 360 K. In the absence of the jet, this configuration ensures a spatially uniform and temporally stable surface temperature, with a root-mean-square temperature fluctuation over the surface of less than 0.02 K, as determined from an average over 100 IR thermography images (see below). Under jet impingement, the temperature variation across the front surface remains below 1.5 K for all experimental conditions considered. The resulting thermal boundary condition therefore closely approximates an isothermal Dirichlet condition, while still enabling accurate determination of the surface temperature distribution. The temperature of the front surface (impingement side) is measured with an infrared camera (InfraTec ImageIR 9480 or VarioCam HD, see Fig. 1). To increase the sensitivity of the temperature measurement, the aluminum wall is coated with a thin, homogeneous layer of paint with high thermal emissivity (see below).

Thermal-image levels have been converted to surface temperature by means of a pixel-wise calibration. Fig. 2 shows exemplary calibration

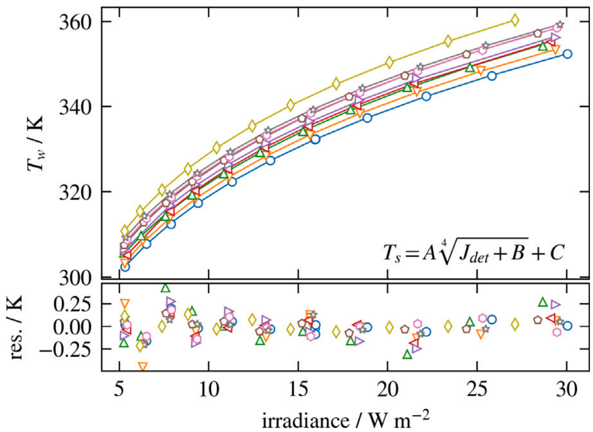

Fig. 2. Pixel-accurate IR calibration curves (top) exemplary for the image pixel in the center of the wall. The different curves correspond to independent calibrations before each individual measurement series. For a clearer representation, the curves have been shifted against each other by 1 °C in each case. The residuals (bottom) are typically on the order of 0.13 K (root-mean-square).

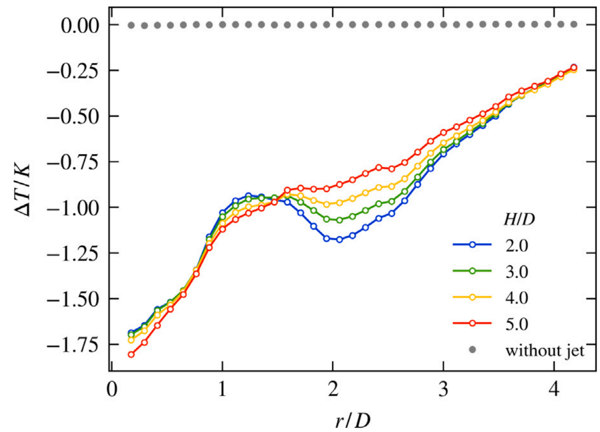

Fig. 3. Radial distribution of wall surface temperature with and without jet at different distances between nozzle and wall (smooth wall, Re = 30 000, T_{jet} = 293 K, T_{wall} = 333 K). Shown are temperature changes relative to the outermost edge of the wall.

curves for the pixel of the camera that images the center of the wall, obtained prior to each measurement campaign. For the calibration, the impingement plate is uniformly heated to temperatures ranging from 303 K to 353 K in the absence of a jet, while reference images are recorded using the IR camera. The calibration curves are generated by fitting the prescribed surface temperature as a function of the measured irradiance, individually for each pixel [40,41].

This in-situ, pixel-by-pixel calibration procedure inherently mitigates radiometric artefacts associated with surface roughness. Specifically, rough surfaces can exhibit an enhanced effective emissivity due to the so-called cavity effect, whereby multiple reflections within surface asperities increase emitted radiation. By calibrating each pixel in the exact measurement configuration using known isothermal states, the recorded radiative signal is directly converted into the true temperature. This procedure automatically incorporates local emissivity variations due to surface morphology and thus prevents roughness-induced emissivity effects from appearing as temperature errors in later measurements.

Since the IR camera looks at the wall at an oblique angle, the images are subject to perspective correction via a projective transformation [42]. This transformation is derived by mapping a set of predefined reference points on the impingement plate, as observed in the image, to their corresponding physical coordinates in the plane of the plate using the scikit-image software library [43]. Calibration is repeated every day before each individual series of measurements, with the IR camera repositioned in each case to account for systematic errors in alignment and perspective correction. From the residuals of all pixels and measurements we estimate the absolute single-pixel accuracy to be about ±0.13 K (root-mean-square deviation).

Fig. 3 shows the variation in surface temperature difference ΔT (local temperature compared to the temperature at the rim of the wall) with and without jet (T_{jet} = 293 K), averaged over 1000 IR images and along the circumference of the wall, at different distances between the nozzle and the wall (H/D = 2, 3 and 4). Without a jet, the surface temperature is constant and homogeneous over the entire surface. In the case of jet impact, the temperature reduction is greatest near the stagnation point and decreases toward the edge of the wall, with a secondary peak at approximately $r/D \approx 2$, similar to the corresponding Nusselt number distribution from the literature (see, e.g., [4,21,24,27,44,45]). As expected, the characteristics of the secondary peak in the temperature profile located at $r/D \approx 2$ change with the distance between the nozzle and the wall, confirming that the surface temperature measurements are suitable and sufficiently sensitive to capture these effects.

The fluid-side heat transfer coefficient $h(r)$ at different radial positions

$$h(r) = \frac{\dot{q}_c(r)}{T_w - T_{jet}}, \tag{1}$$

is used to derive Nusselt number distributions

$$Nu(r) = \frac{h(r)D}{k_{jet}}. \tag{2}$$

Here, $\dot{q}_c$ is the convective heat flux (averaged in time and in circumferential direction), T_w the measured wall temperature and k_{jet} the thermal conductivity of the jet-fluid (air). Note that in Eq. (1), T_{jet} has been adopted as the adiabatic wall temperature. This assumption is justified within the scope of the present study, as the flow is subsonic and the jet temperature matches that of the ambient environment [38,46].

The convective heat flux $\dot{q}_c$ is resolved from the steady-state energy balance on the gradient sensor. Assuming no internal heat generation and a constant thermal conductivity k, the three-dimensional unsteady heat conduction (Fourier–Biot) equation is given by

$$\rho c_p \frac{\partial T}{\partial t} = k\left(\frac{\partial^2 T}{\partial z^2} + \nabla^2 T\right), \tag{3}$$

where $\nabla^2 = \partial^2/\partial x^2 + \partial^2/\partial y^2$ denotes the Laplacian in the x–y plane; ρ, c_p and k are the density, heat capacity and thermal conductivity, respectively. Assuming a steady-state sensor, the transient term ($\partial T/\partial t = 0$) vanishes. Within the framework of a two-dimensional sensor approximation and after integration over the sensor thickness $z \in [0, s]$, where $z = 0$ is the position of the front surface, one obtains:

$$-k\left.\frac{\partial T}{\partial z}\right|_{z=s} = -k\left.\frac{\partial T}{\partial z}\right|_{z=0} + k\int_0^s \nabla^2 T\, dz \tag{4}$$

with the individual contributions representing:

- heat supplied by the thermal oil at the back wall,

  $$\dot{q}_w = -k\left.\frac{\partial T}{\partial z}\right|_{z=s},$$

- heat leaving the sensor through convection and radiation at the front surface,

  $$\dot{q}_c + \dot{q}_r = -k\left.\frac{\partial T}{\partial z}\right|_{z=0},$$

- tangential (in-plane) conduction within the sensor,

  $$\dot{q}_t = k\int_0^s \nabla^2 T\, dz.$$

This leads to the following two-dimensional steady-state energy balance equation:

$$\dot{q}_w = \dot{q}_c + \dot{q}_r + \dot{q}_t \tag{5}$$

In Eq. (5), $\dot{q}_w$ is the measured local heat flux from the thermo-oil to the sensor, $\dot{q}_r$ is the radiative heat flux from the wall surface to the ambient surroundings, and $\dot{q}_t$ accounts for the effect of tangential conduction inside the wall, i.e. parallel to the wall surface [38,39,47]. No other thermal losses are included in the model, as the sensor is thermally isolated from its support. All these quantities are considered as time-averaged and local (i.e. dependent on r) and are derived from the measured wall temperature.

The local heat flux $\dot{q}_w$ through the back wall is estimated from:

$$\dot{q}_w \approx \overline{h}_w \left(\overline{T}_{\text{oil}} - T_w\right), \tag{6}$$

where $\overline{T}_{\text{oil}}$ is the temperature of the thermo-oil averaged over time and $\overline{h}_w$ is the spatially averaged heat transfer coefficient between the oil and the wall. Here, $\bar{h}_w$ accounts for both the convection of the solid/oil and the conduction through the solid. In Eq. (6) the heat flux is considered positive if the energy flows from the solid surface to the fluid of the impinging jet. The heat transfer coefficient $\overline{h}_w$ is assumed to be independent of spatial location and, considering that the changes in local temperature are small, also independent of the thermophysical state of the wall. $\overline{h}_w$ is experimentally determined by means of an energy balance between the total heat transferred to the wall and the heat loss from the thermal oil:

$$2\pi\overline{h}_w \int_0^R \left[\overline{T}_{\text{oil}} - T_w(r)\right] r\,dr = \dot{V}_{\text{oil}}\rho_{\text{oil}}c_{p,\text{oil}}\Delta T_{\text{oil}} \tag{7}$$

Here $\dot{V}_{\text{oil}}$, ρ_{oil} and $c_{p,\text{oil}}$ are the volume flow rate, density, and specific heat capacity of the thermo-oil, respectively. ΔT_{oil} is the difference between the inlet and outlet temperature of the thermo-oil, which is corrected for thermal losses by measuring the temperature difference at the same nominal wall temperature but without jet. ΔT_{oil} is typically of the order of $\approx$0.3 K with an absolute error of about $\pm$16% due to small periodic variations in the thermostat control loop. Systematic differences in the readings of the two thermocouples that measure the inlet and outlet temperatures of the thermo-oil were measured and accounted for in an independent calibration measurement without jet impingement. Together with the remaining uncertainties in the flow rate of the thermal oil and the very simple model applied here, we expect an absolute accuracy of the wall heat flux measurements of $\lesssim\pm$20% (3σ confidence interval), depending on the measurement conditions, as derived from the variation between repeated measurements (c.f. Fig. 6).

The radiative heat flux $\dot{q}_r$ is calculated under the assumption that the ambient surrounding and impingement surface are a black and gray body, respectively [38,46]:

$$\dot{q}_r = \epsilon\sigma\left(T_w^4 - T_{amb}^4\right), \tag{8}$$

where σ is the Stefan–Boltzmann constant, ϵ the emissivity of the impingement surface ($\epsilon = 0.95$) and T_{amb} the ambient temperature in the air-conditioned laboratory. The emissivity of the impingement surface was determined experimentally using IR images under ambient conditions by comparing it with the manufacturer's camera calibration on a standard blackbody.

The contribution of tangential conduction is estimated using Fourier's law [38]:

$$\dot{q}_t = -sk_s\zeta\nabla^2 T_w \quad \text{with} \quad \nabla^2 T_w = \frac{\partial^2 T_w}{\partial r^2} + \frac{1}{r}\frac{\partial T_w}{\partial r} \tag{9}$$

Here, s and k_s are the thickness and thermal conductivity of the wall, and the Laplacian is expressed directly in radial coordinates, taking into account the rotational symmetry. ζ is a correction factor that accounts for the finite thickness of the wall. If there is no temperature gradient between the front and back of the wall, as is usually the case with heated thin-foil sensors, $\zeta = 1$ [38,46]. In other words, the tangential heat flux does not change over the thickness of the wall. The gradient sensor used here has a thickness of $s = 1.5$ mm (smooth wall). Since it is made of aluminum (AlSi10Mg), the Biot number is kept as low as possible and is estimated at $Bi \approx 0.075$, but temperature gradients in the z direction cannot be avoided. Moreover, the evaluation of local heat flux $\dot{q}_w$ presumes that the temperature on the rear side ($\bar{T}_{oil}$) remains constant, suggesting the absence of tangential heat conduction in that area. Under the assumption that the contribution of tangential heat conduction vanishes linearly with the thickness of the wall – similar to the quasi-linear temperature gradient perpendicular to the wall surface [38] – a correction factor of $\zeta = \frac{1}{2}$ is derived.

With regard to the tangential conductivity correction, the greatest difficulty lies in obtaining accurate and meaningful first- and second-order gradients from noisy experimental data. Azimuthal averaging over the circumference of the circular wall helps to reduce the deviations between neighboring data points, but for small values of r, a noticeable scatter is unavoidable due to the smaller number of measurement points along the circumference. Furthermore, the first derivative $\partial T_w/\partial r$ must be proportional to r for $r \to 0$ to avoid a singularity in the evaluation of the Laplacian in Eq. (9). In this work, higher-order smoothing splines with automatic parameter selection (HISAPS) and a penalty for the 4th derivative are used to fit the experimental surface temperature profile using B-spline basis functions [48]. Taking advantage of the axial symmetry, the fit is subject to the constraints $\left(\partial T_w/\partial r\right)_{r=0} = 0$ and $T_w(r) = T_w(-r)$. Mirroring the experimental data at $r = 0$ before the fit helps satisfy the constraint for the first derivative. As an example, Fig. 4 shows the fitted temperature profile, the components with the first and second derivatives, and the complete Laplacian for $Re = 30\,000$ and $H/D = 2$. The two data points closest to the symmetry axis were discarded for all data sets due to the inherent scattering near $r = 0$ mentioned above. Overall, and taking into account the measurement uncertainty, the smoothing spline fits the temperature profile quite well and provides plausible derivatives.

The wall heat flux $\dot{q}_w$, the radiative heat flux $\dot{q}_r$ and the tangential heat conduction contribution $\dot{q}_t$ are evaluated locally using the spatially resolved wall surface temperature $T_w(r)$. Fig. 5 illustrates the individual heat flux quantities and the derived convective heat flux $\dot{q}_c$ for one exemplary case using the smooth wall. Due to the low temperature variation on the wall surface and the much larger temperature difference between the wall surface and the environment, the radiative heat flux is almost constant, but leads to a non-negligible offset, especially at lower Reynolds numbers, i.e. lower heat flux values. The tangential conduction correction, on the other hand, restores the local structure of the heat flux distribution by making the 'peaks' higher and the 'valleys' deeper. The Nusselt number distribution is determined from the convective heat flux derived in this way in combination with Eq. (2).

With regard to measurement uncertainties, the parameter exerting the greatest influence on the absolute accuracy is the determination of the heat supplied by the thermal oil at the back wall, $\dot{q}_w$ (Eqs. (6) and (7)). This quantity is predominantly governed by the temperature difference ΔT_{oil} between the inlet and outlet of the temperature-control spiral, which is relatively small, with an average value of approximately 0.3 K and an associated uncertainty of about $\pm$16% (see above). This sensitivity is directly manifested in the variation of the Nusselt number distributions among different measurement series, as the overall heat balance is dominated by the heat flux from the thermal oil to the working fluid. Radiative heat transfer plays only a minor role at the wall temperatures considered in this study and depends solely on the wall surface temperature, for which the overall uncertainty is significantly lower (c.f. Fig. 2). The correction for tangential conduction depends primarily on the shape of the wall temperature distribution, which is reconstructed using a higher-order smoothing spline. The uncertainty associated with this reconstruction is estimated to be less than

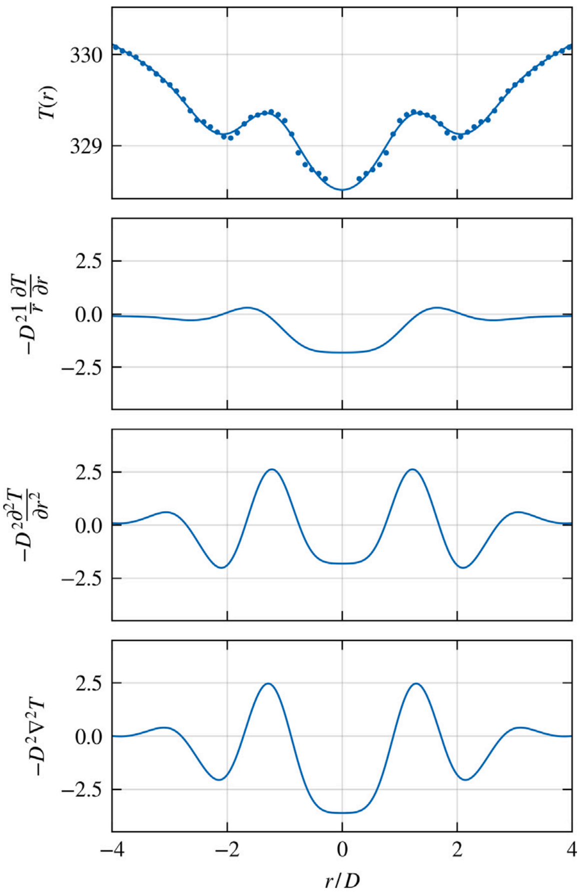

Fig. 4. Illustration of first- and second-order temperature gradients obtained by fitting the experimentally measured temperature profiles, indicated by points, with a higher-order smoothing spline (smooth wall, Re = 30 000, $H/D = 2$, $T_w = 333$ K, $T_{jet} = 293$ K).

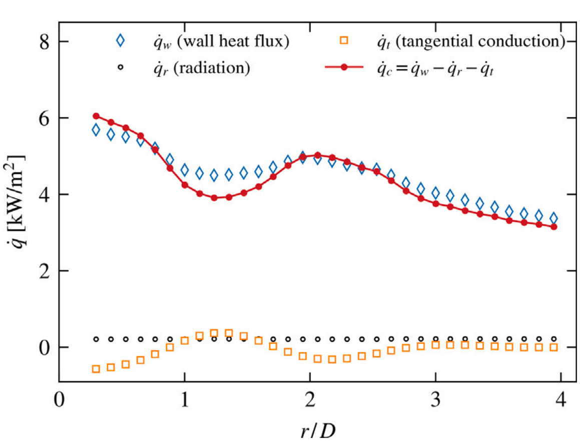

Fig. 5. Different contributions to the calculation of the convective heat flux for obtaining Nusselt number distributions (Re = 30000, H/D = 2, smooth wall).

±5%, based on repeated spline fits initialized from different starting conditions. Since the tangential conduction correction contributes less than 15% to the total heat flux, the resulting reconstruction error is considered to be practically negligible.

In the presentation of the experimental data, either the 99.7% confidence interval is reported, derived from repeated measurements using Student's t-distribution, or all individual data points obtained for a given operating condition (wall type, Reynolds number, nozzle-to-wall distance) are displayed as small markers together with the corresponding mean value. When interpreting these confidence intervals, it must be emphasized that statistical measures such as the variance are not robust descriptors of distributional spread and are highly sensitive to outliers. Consequently, apparently large "error bars" may arise from a small number of outlying observations, which become evident when the individual data points are plotted. In view of the considerable scatter reported in the literature for nominally identical conditions (as discussed in the subsequent section), these apparent outliers were retained in the analysis in order to represent the associated uncertainties and data dispersion in a transparent and explicitly traceable manner.

The spatial resolution of the gradient sensor is governed by the camera optics and detector characteristics, but also by the thermal response of the sensor wall. In the present setup, the effective pixel resolution of the thermograms is approximately 0.65 mm, resulting from the camera sensor size, the infrared field of view, and the perspective correction required by the non-normal viewing angle of the plate. The two-dimensional temperature fields are subsequently processed by radial averaging, using a radial bin width of 2.9 mm.

Beyond these acquisition-related constraints, lateral thermal diffusion within the wall limits the smallest spatial scales of heat-flux fluctuations that can be resolved. This effect can be quantified by introducing a spatial modulation transfer function (MTF), derived from the steady-state heat conduction equation for a thermally thick wall subjected to a harmonic surface heat-flux perturbation of wavelength λ. The MTF describes the attenuation of the resulting surface temperature modulation relative to the ideal one-dimensional response in the absence of lateral conduction. For one-dimensional heat-flux variations, representative of the axisymmetric configuration considered here, the temperature modulation transfer function reads

$$\mathrm{MTF} = \frac{\lambda/s}{2\pi}\tanh\left(\frac{2\pi}{\lambda/s}\right).$$

This expression shows that spatial temperature fluctuations are increasingly attenuated as the wavelength approaches the slab thickness. Using the conventional 50% amplitude attenuation criterion, the practical resolution limit is found at $\lambda/s \approx 3$, corresponding to a minimum resolvable wavelength of approximately 4.5 mm for the present sensor. This intrinsic thermal resolution limit is well below the characteristic spatial scales of the heat-transfer structures induced by the impinging jet, which are of the order of one nozzle diameter (25 mm), and is comparable to the radial bin size used in the post-processing. Therefore, the thermal response of the sensor wall and the post-processing of the images do not limit the ability of the present measurements to resolve the relevant heat-transfer features.

Notice that this resolution limit arises from the presence of the tangential conduction. For reduced wavelengths of the heat flux features, also the proposed correction (Eq. (9)) is affected, introducing further errors due to the increasing discrepancy between the actual distribution of temperature in the slab thickness and the quasi-linear hypothesis. This error can be estimated as

$$\dot{q}_t \approx \dot{q}_{t,lin}\left(1 - \frac{\pi^2 s^2}{3\lambda^2}\right),$$

where $\dot{q}_t$ and $\dot{q}_{t,lin}$ are the tangential conduction term from the actual temperature profile and from the linearized temperature profile, respectively. When the nozzle diameter is adopted as the characteristic length scale for representing the features of the Nusselt number distribution, the resulting error is less than 2% for the smooth wall with a thickness of $s = 1.5$ mm.

The Nusselt number distribution on rough surfaces is determined analogously, with the plate thickness s approximated as the distance from the back side of the impingement plate to the mean roughness height. For the two configurations investigated, the average plate thicknesses are $s = 2.0$ mm ($k_{99}/D = 0.04$) and $s = 3.0$ mm ($k_{99}/D = 0.12$), respectively. The front surfaces of the 3D-printed rough impingement plates [13] were coated with a thin layer (<50 μm) of high-emissivity paint, identical to that applied to the smooth reference wall. Visual inspection confirmed that the coating did not induce any significant alteration of the surface topography, such as paint accumulation within the troughs of the roughness profile. For rough surfaces, the impingement plates were additionally rotated by a few degrees about the jet axis prior to each calibration and subsequent measurement campaign. This procedure served two purposes: (1) to vary the orientation of the roughness elements relative to the IR camera, thereby mitigating the influence of individual features on the measured temperature fields, and (2) to improve statistical reliability by averaging results over multiple orientations.

An important aspect that needs to be highlighted is the fitness of the present sensor model to the solution of the heat flux also with a rough slab geometry. While the roughness, introducing local variations of the thickness, can produce variations of the temperature within the slab with respect to the equivalent flat slab, these variations would produce an temperature modulation with similar wavelength than the roughness over the temperature distribution which would be observed on a flat slab for the same heat flux perturbation. Therefore, if sufficient separation is provided between the length scales of the roughness and heat flux features, such as in the present experiment, the equivalent temperature distribution of a flat slab can be retrieved by filtering the high frequency component due to the rough geometry, thus allowing to solve for the heat flux with minimal distortions.

4. Results

4.1. Nusselt number distribution on smooth impingement plate

This section examines heat transfer measurements over smooth walls with the primary objective of validating the accuracy and robustness of the gradient-based heat flux sensor employed in this study. Agreement with numerical predictions, as well as with established experimental data and correlations from the literature for canonical smooth-wall configurations, demonstrates the reliability of the measurements and establishes a solid experimental baseline. Such validation is a necessary prerequisite before extending the application of the sensor to more complex wall geometries, such as rough surfaces, where accurate local heat-flux measurements are crucial and independent reference data are not available.

The evaluated Nusselt number distribution at Re = 5000 and Re = 10 000 is shown in Fig. 6 in comparison to numerical data based on direct numerical simulation (DNS) in which temperature is treated as a passive scalar [4,49]. The experimental data are shown with error bars representing the 99.7 % confidence interval of independent measurements, calculated using Student's t-distribution. Fig. 6(a) displays the results at Re = 5000. While experiments are carried out in air, which corresponds to a Prandtl number of Pr = 0.72, DNS data are presented for Pr = 0.72 and Pr = 1.0. A very good agreement between experiment and DNS is found for Pr = 0.72, while the larger Prandtl number case, Pr = 1.0, leads to a larger Nu throughout the plate. Similar results are obtained under rough-wall conditions, although they are not shown here since roughness has only a minor effect at low Reynolds numbers [15]. In the DNS study [49] a fully developed pipe flow provides the inflow condition of the jet, and a constant Dirichlet boundary condition is imposed on the impingement wall for the passive scalar, thus providing test conditions comparable to the experiments, where temperature variation across the impingement surface are small (≈1.5 K). Fig. 6(b) corresponds to Re = 10 000 where numerical reference data at Pr = 0.72 are not available. The DNS results for Pr = 1.0 are in good qualitative agreement with the present experimental results, slightly overestimating the measured Nu distribution likely due to the higher Pr.

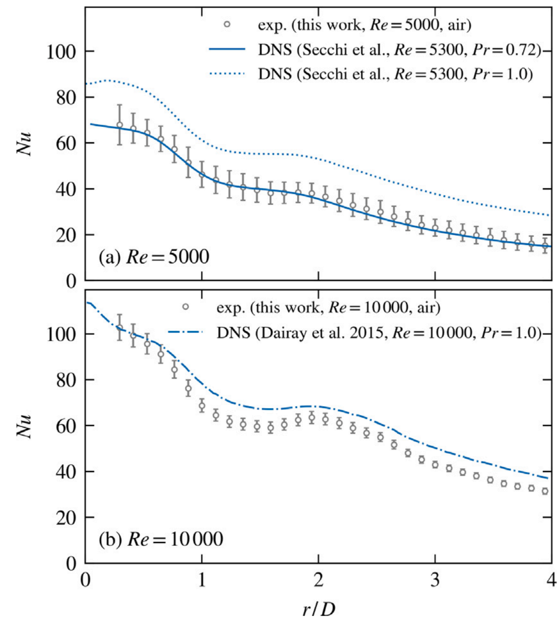

Fig. 6. Comparison of experimentally obtained Nusselt number distributions on the smooth reference plate with DNS results [4,49] for (a) Re = 5000 and (b) Re = 10 000. The error bars represent the 99.7 % confidence interval, based on series of independent measurements consisting of 4 measurements for Re = 5000 and 21 measurements for Re = 10 000, respectively.

For Reynolds numbers in the range 10 000 ≤ Re ≤ 25 000, a comparison with experimental data from the literature for H/D = 2 is presented in Fig. 7. Considerable scatter between the various measurement campaigns is evident, which highlights the uncertainties and challenges involved in measuring Nusselt number distributions, even on a smooth surface. The closest agreement with the present data is found with the measurements by Lee and Lee [21] for r/D > 0.5. The discrepancies observed near the stagnation point are most likely related to differences in inflow conditions and turbulence levels [4,50,51]. For nozzle-to-plate spacings and Reynolds numbers comparable to those investigated here, elevated turbulence levels in the vicinity of the jet core tend to increase the stagnation-point Nusselt number [52]. Moreover, jets issuing from fully developed turbulent pipe flow exhibit mean Nusselt number distributions with a global maximum at the stagnation point, whereas low-turbulence convergent nozzles cause this global maximum to be shifted radially [4,50].

The influence of Reynolds number on the present measurements is shown in Fig. 8(a) for the smallest nozzle-to-plate distance investigated here (H/D = 2). With increasing Reynolds number, the Nusselt number clearly rises, and the secondary peak around r/D = 2 becomes significantly more pronounced. Jambunathan et al. [53] suggested that the heat transfer increase in the stagnation region scales with $Nu_{stag} \propto Re^{0.5}$, following an analysis of Sibulkin [54] for laminar impinging flow and the related heat transfer in the stagnation region. Consequently, the smooth-wall heat transfer data are plotted in terms of $Nu/Re^{0.5}$ in Fig. 8(b). Consistent with this scaling, the data for 5000 ≤ Re ≤ 30 000 collapse in the region $r/D \leq 1$. In the wall-jet region, $1 < r/D < 4$, $Nu/Re^{0.5}$ increases with Re. The strengthening of the secondary peak is most likely associated with the development of more intense large-scale toroidal structures in the jet shear layers and their interaction with the near-wall flow.

The impact of a larger nozzle-to-plate distance H/D on Nu-distribution is visible in Fig. 9, which shows $Nu/Re^{0.5}$ for six different Reynolds numbers and four different H/D. The secondary peak in Nu around r/D = 2 decreases with increasing H/D, consistent with existing observations in the literature [21,25,44,55,56]. At the

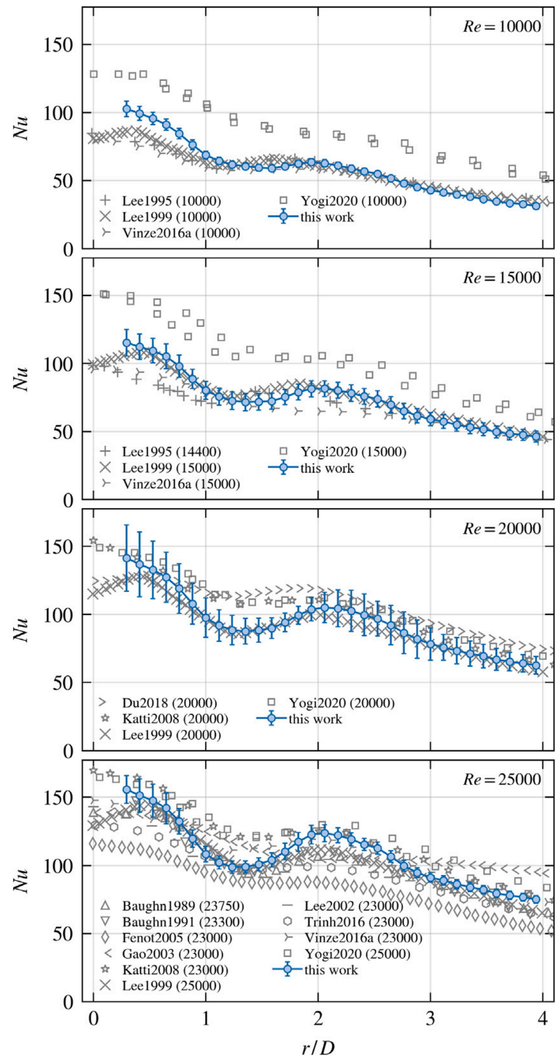

Fig. 7. Comparison of the Nusselt number distributions at $H/D = 2$ obtained in the present study for a smooth wall with corresponding data reported in the literature, as a function of the Reynolds number. The values in parenthesis are the actual Reynolds number used in the respective study. Error bars represent the 99.7 % confidence interval, calculated using Student's t-distribution.

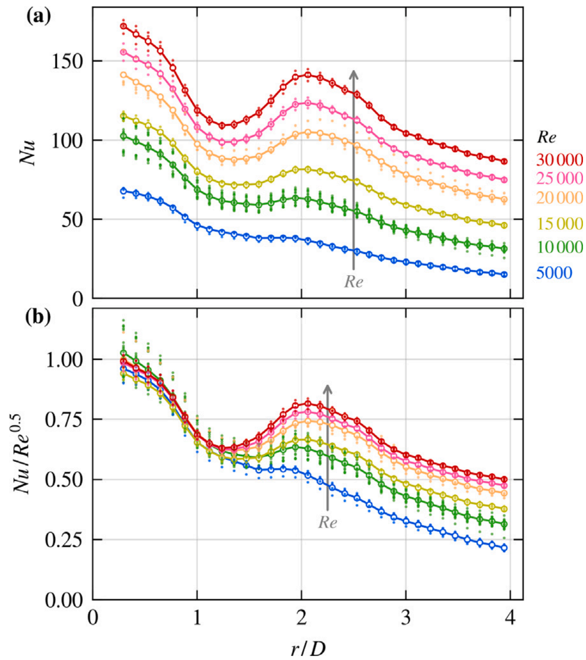

Fig. 8. (a) Nusselt number distribution over the smooth reference plate for a nozzle-to-plate distance of $H/D = 2$ at various Reynolds numbers ($5000 \leq Re \leq 30\,000$). (b) Same distribution scaled by $Re^{0.5}$ (see text for details). Lines and large, open symbols represent the average of all measurements at a specific Reynolds number, while the small dots illustrate the variations between repeated measurements.

same time, the local minimum of Nu around $r/D = 1.2$ is also less pronounced with increasing H/D. The data suggest that Nu monotonically decreases in the radial direction for lower Re and larger H/D, indicating a reduced relevance of large-scale toroidal flow structures for the radial heat transfer distribution. This trend is in agreement with literature data [53]. In the region $r/D < 1$ the data show hardly any dependence on H/D, suggesting that the correlation $Nu \sim Re^{0.5}$ holds reasonably well in the impingement region, irrespective of Re and the distance from the nozzle to the plate for the present data set.

To further investigate the relationship between Nu and Re as a function of radial distance, the exponent β in the correlation $Nu \sim Re^{\beta}$ is determined by performing a linear fit of $\ln(Nu)$ versus $\ln(Re)$ and extracting the slope. The resulting values of β are presented in Fig. 10. The standard deviation of the fitted slope is approximately 0.02, irrespective of the radial position. β increases monotonically with r/D from 0.5 in the stagnation region and approaches a value of approximately unity at $r/D = 4$ for all H/D. At intermediate radial positions ($1 \lesssim r/D \lesssim 3.5$), a systematic dependence on H/D emerges, with the highest values for β at the largest nozzle-to-plate distance. The observed dependence of β on both radial distance from the stagnation point and nozzle-to-plate distance is in qualitative agreement with the correlation proposed by Jambunathan et al. [53]. Their empirical expression for β, obtained from a fit to literature data covering various nozzle geometries (including elliptic nozzles and orifices), is shown as lines in Fig. 10 for comparison. While the overall trends are similar, noticeable quantitative discrepancies between the present results and the proposed correlation are evident.

In the stagnation region, the correlation proposed by Jambunathan et al. [53] does not converge toward $\beta = 0.5$, but instead predicts larger values that, in contrast to the experimental observations, exhibit a strong and systematic dependence on the nozzle-to-plate distance, ranging from 0.5 to 0.65. This discrepancy may be attributed to the pronounced influence of nozzle geometry on heat transfer in the stagnation region. An increase in turbulence intensity within the jet core with increasing nozzle-to-plate distance and Reynolds number may account for the elevated β values observed in this region. At a radial position of $r/D = 4$, both the literature correlation and the present measurements indicate that the local heat transfer is again independent of the nozzle-to-plate spacing. This qualitative independence of H/D is also evident from the Nusselt number distributions in Fig. 9, where the values of $Nu/Re^{0.5}$ at $r/D = 4$ and a fixed Reynolds number are nearly identical for all four investigated nozzle-to-plate distances. Nevertheless, the present data, obtained for fully developed turbulent pipe flow at the nozzle exit, reveal an almost linear increase of β with radial distance for $3 < r/D < 4$, whereas the correlation by Jambunathan et al. [53] predicts an asymptotic approach toward $\beta = 0.8$.

4.2. Nusselt number distribution on rough impingement plates

In the following, we address the relevance of surface roughness for impinging jet heat transfer. Particular emphasis is placed on how the introduction of surface roughness affects the local convective heat transfer and, consequently, the spatial distribution of the Nusselt number. To this end, the radial distribution of the local Nusselt number,

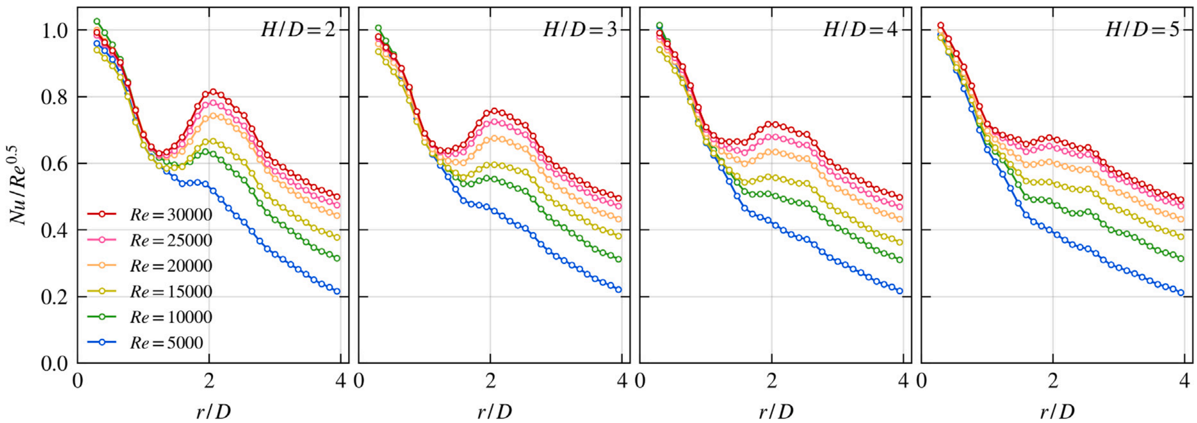

Fig. 9. Influence of Reynolds number and nozzle-to-plate distance on the scaled Nusselt number distribution ($Nu/Re^{0.5}$) over the smooth reference plate. Lines and symbols reflect the average of all measurements under the respective conditions.

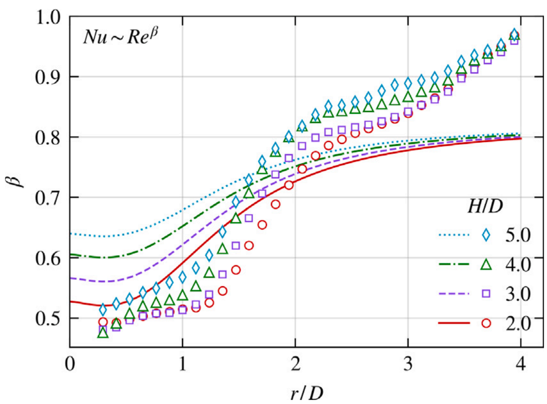

Fig. 10. Variation of the exponent β in the correlation $Nu \sim Re^{\beta}$ as a function of radial position and plate-to-nozzle distance on the smooth reference plate. Symbols denote the β values obtained in the present study, while the lines represent the empirical correlation proposed by Jambunathan et al. [53].

$Nu(r)$, is investigated systematically for the two representative roughness configurations introduced in Section 2, hereafter referred to as the small and large roughness cases. By comparing these two cases with each other (and, where appropriate, with the smooth reference surface), we aim to quantify the influence of surface roughness on the heat transfer performance.

The corresponding results are presented in Fig. 11(a) and (b), which depict the radial Nusselt number distributions for the plates with small ($k_{99}/D = 0.04$) and large roughness ($k_{99}/D = 0.12$) at a nozzle-to-plate distance of $H/D = 2$, and for the same Reynolds numbers as in the smooth-wall case (compare Fig. 8a). As previously, the large symbols and solid lines denote the average over all realizations at a given Reynolds number, while the small dots indicate the scatter between repeated measurements. The overall level of scatter is comparable to that observed for the smooth reference configuration. Fig. 11(c) and (d) display the same distributions, but scaled with $Re^{0.5}$.

Similar to the smooth case, the heat transfer expressed in terms of Nu increases at all radial positions with increasing Re. However, the collapse of $Nu/Re^{0.5}$ in the stagnation region observed for the smooth surface in Fig. 8(b) is not observed for the rough surfaces; see Fig. 11(c) and (d). This indicates that the heat-transfer enhancement in the impingement region for rough surfaces does not follow the same scaling $Nu_{stag} \propto Re^{0.5}$ as for the smooth surface, but instead exhibits a stronger power-law dependence on Re. A plausible explanation is an increase in turbulence intensity in this region caused by a Re-dependent interaction of the impinging jet with individual roughness elements. The large roughness leads to larger values of Nu at all radial positions compared to the small roughness. However, the magnitude of Nu at the lowest Re for both rough surfaces is similar to the smooth wall. This observation is in agreement with numerical results at $Re = 5300$ [15].

Comparing Figs. 8 and 11, it is interesting to note that the radial distribution of Nu is substantially modified by roughness at higher Reynolds numbers. In particular, the secondary peak of Nu that is clearly visible for the smooth surface at $Re \geq 10\,000$ and $H/D = 2$ is much less pronounced for the rough surfaces. It only appears weakly at $Re = 15\,000$ and $Re = 20\,000$. At the highest Reynolds numbers investigated, no secondary peak is observed on the rough surfaces; instead, Nu remains nearly constant up to $r/D \approx 1.2$ and then decreases monotonically up to $r/D = 4$.

For hydraulically smooth impingement plates, the amplitude of the secondary peak in the mean Nusselt number distribution increases for increasing the jet Reynolds number and for decreasing the nozzle-to-plate distance [18,21,50,52]. These observations are consistent with the present smooth-wall measurements reported in Fig. 9. According to the phenomenological scenario presented by Dairay et al. [4], the secondary peak arises due to the presence of azimuthal distortions in the large-scale toroidal vortices that convect radially in the near-wall vicinity. These large-scale structures, usually referred to as secondary vortices, are induced by primary large-scale toroidal vortices originating from Kelvin–Helmholtz instabilities in the shear layers of the free and the wall jets. The irregular shape of the secondary vortices causes the presence of angular locations where these vortical structures lie closer to the wall, thus determining spots of intense local wall heat transfer. In addition, radially-elongated structures form in the neighborhood of these spots, further contributing to the enhancement of the local wall heat transfer.

For rough wall impingement plates, no such a detailed phenomenological scenario has been investigated in the literature. The present measurements suggest that roughness plays a detrimental role in the appearance of the secondary peak, especially for the large roughness case reported in Fig. 11b. However, due to the lack of simultaneous flow field and wall heat transfer measurements, any explanation of the roughness effects on the existence of a secondary peak in the mean Nusselt number distribution can only be speculative at this time and future investigations are required to address this question.

Fig. 12 shows the ratio of Nusselt number for rough and smooth surfaces for varying nozzle-to plate distance and over the entire investigated Reynolds number range. As before, the lines indicate ensemble-averaged values across all realizations for a given Reynolds number Re and distance H/D, while the dots show the corresponding individual data points. Some conditions exhibit more pronounced outliers, which have been intentionally retained to demonstrate the measurement uncertainties. In this representation, a strong increase of Nu by up to

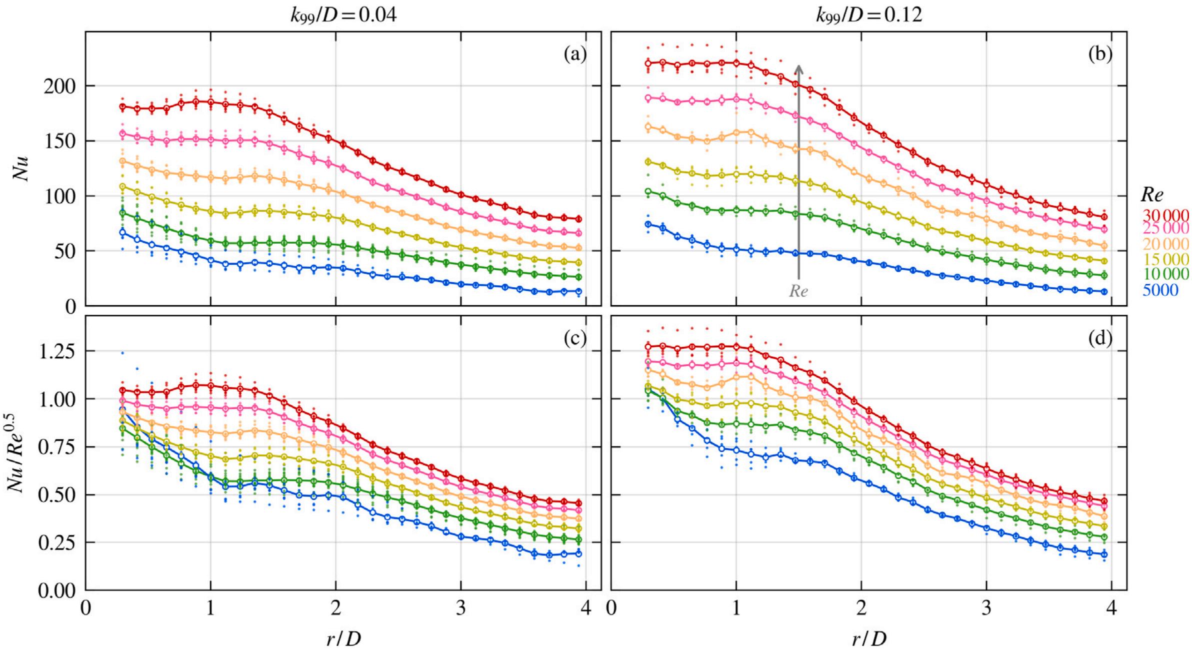

Fig. 11. (a) & (b): Nusselt number distribution over the two plates with small (k_{99}/D = 0.04) and large (k_{99}/D = 0.12) roughness scales for a nozzle-to-plate distance of $H/D = 2$ at various Reynolds numbers ($5000 \leq Re \leq 30\,0000$). (c) & (d): Same distributions scaled by $Re^{0.5}$ (see text for details). Lines and large, open symbols represent the average of all measurements at a specific Reynolds number, while the small dots illustrate the variations between repeated measurements.

a factor of 2 due to roughness at high Re is clearly visible around $r/D \approx 1.2$ which corresponds to the location of the local minimum of Nu on the smooth wall. This effect is found for all investigated H/D with a stronger enhancement of Nu for the large roughness. In contrast to the small roughness, the large roughness also displays a clear local enhancement of Nu at the two lowest investigated Re. The location of maximum heat transfer increase due to roughness appears to slightly shift towards smaller r/D with increasing Re. At $r/D \approx 2$, i.e. the location of the secondary Nu-peak on smooth walls, the ratio $Nu_{\text{rough}}/Nu_{\text{small}}$ is close to one for all investigated flow states for the small roughness (left column of Fig. 12). Slightly larger values are observed for the large roughness for which $Nu_{\text{rough}}/Nu_{\text{small}} \approx 1$ are found for $r/D > 2.5$ with a slight tendency for an extended region of Nu-increase with increasing nozzle-to-plate distance. Overall, a substantial influence of surface roughness on heat transfer is observed for $r/D < 2$, whereas its effect becomes comparatively minor at larger radial distances.

It is interesting to note that Fig. 12 contains a number of data points with $Nu_{\text{rough}}/Nu_{\text{smooth}} < 1$ for the small roughness. This reduction of heat transfer (which is in the order of the experimental uncertainty) appears to exist over the entire plate for the lowest Re. It is consistently found at large radial distances for all Re. This effect might be related to the fact that the presence of roughness changes the near-wall flow conditions and hence the radial development of the wall-jet. Roughness is expected to induce additional drag and hence an increased thickening of the turbulent boundary layer. The same radial locations might therefore correspond to smaller radial flow speeds for the rough surface. However, such an effect is not observed for the large roughness and it deserves further attention in future studies in which heat transfer and flow field measurements should ideally be combined.

5. Conclusion

This study provides the first systematic dataset on heat transfer of turbulent impinging jets on rough surfaces, considering variations in roughness size, Reynolds number, and nozzle-to-plate distance. While the enhancement of convective heat flux due to surface roughness has been extensively studied for boundary layer flows in recent years (see [7,57] for a review), corresponding investigations for impinging jets remain scarce. Previous DNS studies reported negligible effects of roughness on impinging jet heat transfer [15], but these were restricted to low Reynolds numbers due to computational costs. Experimental approaches allow access to higher Reynolds numbers. However, accurate wall heat flux measurements are notoriously challenging and subject to significant uncertainty, also for turbulent boundary layers [33]. Also, non-intrusive heat-transfer measurement techniques with high spatial resolution typically involve the use of an heated-thin-foil sensor, which would not allow the inclusion of surface roughness.

To address this challenge, heat flux measurements were performed using an infrared thermography-based gradient sensor [38] on a temperature-controlled plate. This sensor, which relies on the thermally thick slab hypothesis, provides a solid metallic surface capable of incorporating both smooth- and rough-wall features. The sensor layout and the associated measurement pipeline must, however, be designed with care to avoid the inherent constraints of the thermally thick assumption, particularly regarding spatial resolution. Specifically, for the steady-state sensor, the maximum slab thickness and the largest allowable roughness scale must be chosen in relation to the minimum spatial resolution required to detect heat flux perturbations. Comparison with DNS data in the low-Re range and with data from the literature demonstrate the capability of the proposed methodology to provide accurate spatially-resolved time-averaged measurements of the heat transfer for the present impinging jet experiment. This result opens the way to convective heat transfer measurements on rough surfaces, possibly extending to other flow cases apart for the present impinging jet.

Analysis of smooth-wall data highlights the influence of radial heat conduction in this configuration. The smooth-wall results agree well with selected literature references, despite the considerable scatter among published data, and show excellent consistency with DNS predictions at low Reynolds numbers.

The rough-wall dataset comprises two distinct roughness sizes (small and large) at four nozzle-to-plate distances over a Reynolds number range of $5000 \leq Re \leq 30\,000$. Overall, the data indicate that roughness increases heat transfer of impinging jets significantly once a certain combination of roughness size and Reynolds number

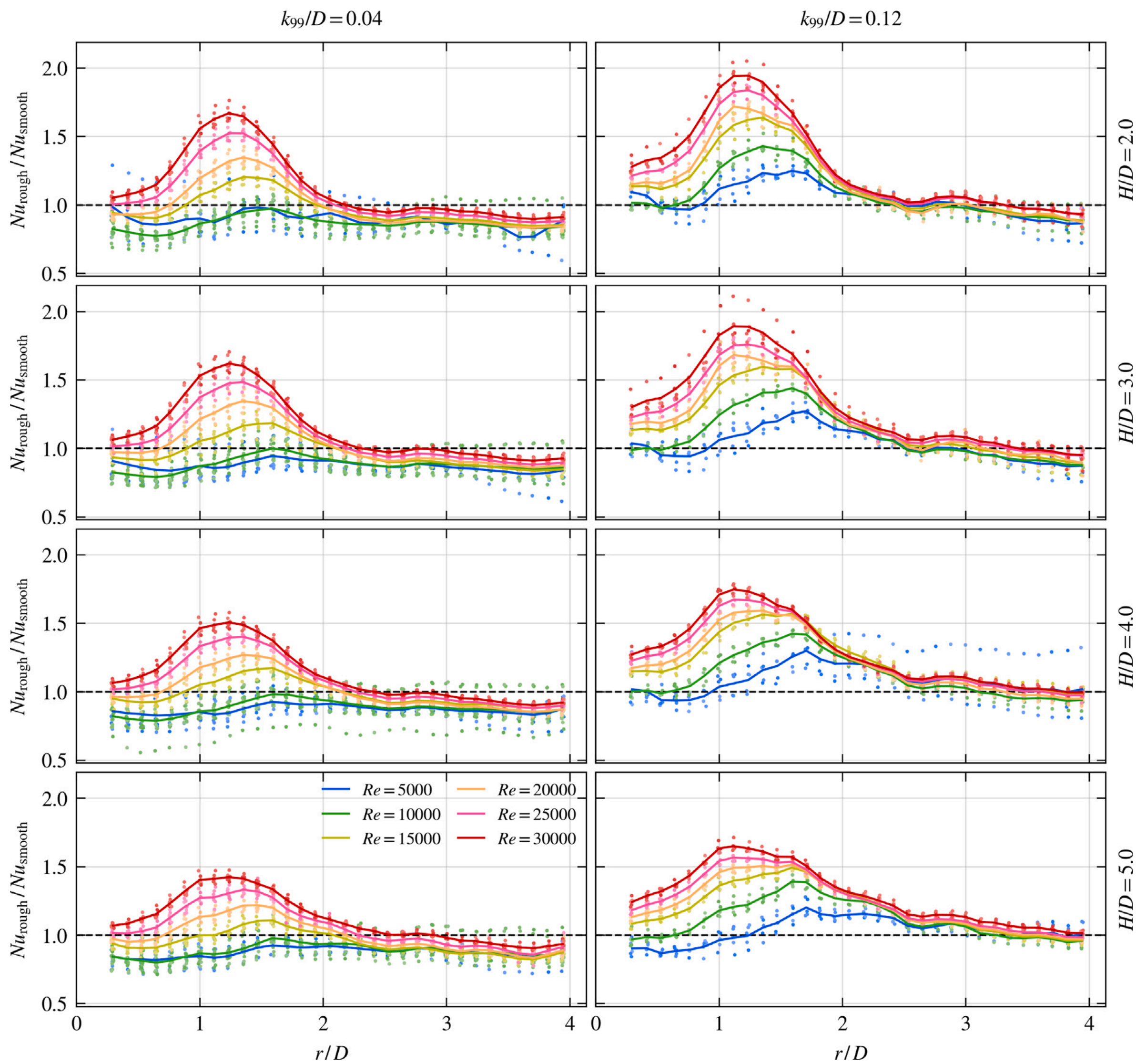

Fig. 12. Radial dependence of the ratio in Nusselt number between the rough plates and the smooth reference case as a function of the Reynolds number and the distance between the nozzle outlet and the impingement plate. Lines denote the ensemble-averaged values over all realizations for a given Reynolds number Re and distance H/D, whereas dots represent the corresponding individual measurements.

is reached. Specifically, an enhancement beyond experimental uncertainty is observed for the large roughness at $Re \geq 10\,000$ and for the smaller roughness at $Re \geq 15\,000$. The radial location of pronounced heat transfer corresponds to regions where the effective wall shear stress is expected to be high, starting near $r/D \approx 1$ (where the wall jet forms) and extending to $r/D \approx 2$. In future work, the question of how to obtain a local effective wall shear stress for the rough wall impinging jet configuration (which is required to deduce the viscous length scale δ_v and hence e.g. a classification of the onset of departure from a hydraulically smooth regime) remains to be addressed. For the present data, the radial extent in which heat transfer increase due to roughness is present, is slightly larger for the large roughness. A modest heat transfer increase is also detected in the stagnation region for the large roughness. For the smaller roughness, uncertainties prevent clear differentiation from the smooth-wall reference in this region.

The main finding of the present study is that, at higher Reynolds numbers, rough surfaces do not exhibit the characteristic secondary peak in the radial Nusselt number distribution known for smooth-wall impinging jets. In contrast, the Nusselt number distribution exhibits a bell-shaped profile. This change in shape is mainly related to an increase of Nu at the radial location where a local minimum of Nu is located on the smooth wall. Further insight into the mechanisms responsible for this different behavior will require combined flow-field, direct wall-shear-stress, and heat-transfer measurements, which will be the subject of future studies.

CRediT authorship contribution statement

Thomas Häber: Writing – original draft, Visualization, Validation, Methodology, Formal analysis, Data curation. **Sebastian Moosmayer:** Visualization, Investigation, Formal analysis, Data curation. **Francesco Secchi:** Writing – original draft, Software, Investigation, Conceptualization. **Marco Raiola:** Writing – original draft, Methodology, Formal analysis. **Davide Gatti:** Writing – review & editing, Supervision, Conceptualization. **Dimosthenis Trimis:** Supervision, Methodology, Funding acquisition. **Rainer Suntz:** Writing – review & editing, Supervision, Project administration, Methodology, Funding acquisition. **Bettina Frohnapfel:** Writing – original draft, Supervision, Funding acquisition, Conceptualization.

Funding sources

This work was supported by the German Research Foundation (DFG) under the Collaborative Research Centre TRR150 (project number 237267381) and the Helmholtz program 'Materials and Technologies for the Energy Transition, Germany' (MTET, 38.03.04). Marco Raiola acknowledges support of the Alexander von Humboldt Foundation.

Declaration of competing interest

The authors declare that they have no known competing financial interests or personal relationships that could have appeared to influence the work reported in this paper.

Data availability

The data will be made available on KITOpen.

References

[1] G.M. Carlomagno, A. Ianiro, Thermo-fluid-dynamics of submerged jets impinging at short nozzle-to-plate distance: A review, Exp. Therm. Fluid Sci. 58 (2014) 15–35, http://dx.doi.org/10.1016/j.expthermflusci.2014.06.010.

[2] N. Uddin, P.T.W. Kee, B. Weigand, Heat transfer by jet impingement: A review of heat transfer correlations and high-fidelity simulations, Appl. Therm. Eng. 257 (2024) 124258, http://dx.doi.org/10.1016/j.applthermaleng.2024.124258.

[3] F. Secchi, D. Gatti, B. Frohnapfel, Energetics of a turbulent impinging jet with passive scalar transport, J. Fluid Mech. (2025) submitted for publication.

[4] T. Dairay, V. Fortuné, E. Lamballais, L.-E. Brizzi, Direct numerical simulation of a turbulent jet impinging on a heated wall, J. Fluid Mech. 764 (2015) 362–394, http://dx.doi.org/10.1017/jfm.2014.715.

[5] M. Raiola, F. Secchi, D. Gatti, J. Kriegseis, B. Frohnapfel, Heat-and momentum-transfer spatio-temporal features in impinging jets using LSE-HPOD, in: S. Hickel (Ed.), Proceedings of the 15th ERCOFTAC Symposium on Engineering Turbulence Modelling and Measurements (ETMM15), ERCOFTAC, Dubrovnik, Croatia, 2025, pp. 632–637, http://dx.doi.org/10.5281/zenodo.17280519.

[6] D. Chung, N. Hutchins, M.P. Schultz, K.A. Flack, Predicting the drag of rough surfaces, Annu. Rev. Fluid Mech. 53 (1) (2021) 439–471, http://dx.doi.org/10.1146/annurev-fluid-062520-115127.

[7] M. Kadivar, H. Garg, Turbulent heat transfer over roughness: A comprehensive review of theories and turbulent flow structure, Int. J. Thermofluids 26 (2025) 100967, http://dx.doi.org/10.1016/j.ijft.2024.100967.

[8] S.V. Ekkad, P. Singh, A modern review on jet impingement heat transfer methods, J. Heat Transf. 143 (6) (2021) 64001, http://dx.doi.org/10.1115/1.4049496.

[9] L.G. Hansen, B.W. Webb, Air jet impingement heat transfer from modified surfaces, Int. J. Heat Mass Transfer 36 (4) (1993) 989–997, http://dx.doi.org/10.1016/S0017-9310(05)80283-2.

[10] W.M. Chakroun, A.A. Abdel-Rahman, S.F. Al-Fahed, Heat transfer augmentation for air jet impinged on a rough surface, Appl. Therm. Eng. 18 (12) (1998) 1225–1241, http://dx.doi.org/10.1016/S1359-4311(97)00100-2.

[11] S.V. Ekkad, D. Kontrovitz, Jet impingement heat transfer on dimpled target surfaces, Int. J. Heat Fluid Flow 23 (1) (2002) 22–28, http://dx.doi.org/10.1016/S0142-727X(01)00139-4.

[12] W. Wu, R. Banyassady, U. Piomelli, Large-eddy simulation of impinging jets on smooth and rough surfaces, J. Turbul. 17 (9) (2016) 847–869, http://dx.doi.org/10.1080/14685248.2016.1181761.

[13] F. Secchi, T. Häber, D. Gatti, S. Schulz, D. Trimis, R. Suntz, B. Frohnapfel, Turbulent impinging jets on rough surfaces, GAMM-Mitt. 45 (1) (2022) 71–89, http://dx.doi.org/10.1002/gamm.202200005.

[14] F. Secchi, D. Gatti, B. Frohnapfel, The wall-jet region of a turbulent jet impinging on smooth and rough plates, Flow, Turbul. Combust. 110 (2) (2023) 275–299, http://dx.doi.org/10.1007/s10494-022-00387-x.

[15] F. Secchi, D. Gatti, B. Frohnapfel, Turbulent jet impingement: Surface roughness effects on wall-heat transfer, in: Proceeding of 10th International Symposium on Turbulence, Heat and Mass Transfer, THMT-23, Rome, Italy, 11-15 September 2023, Begellhouse, 2023, p. 4, http://dx.doi.org/10.1615/ICHMT.THMT-23.970.

[16] H. Schlichting, K. Gersten, Boundary-Layer Theory, Springer, Berlin, Heidelberg, 2017, http://dx.doi.org/10.1007/978-3-662-52919-5.

[17] D.J. Phares, G.T. Smedley, R.C. Flagan, The wall shear stress produced by the normal impingement of a jet on a flat surface, J. Fluid Mech. 418 (2000) 351–375, http://dx.doi.org/10.1017/S002211200000121X.

[18] J.W. Baughn, S. Shimizu, Heat transfer measurements from a surface with uniform heat flux and an impinging jet, J. Heat Transf. 111 (4) (1989) 1096–1098, http://dx.doi.org/10.1115/1.3250776.

[19] J.W. Baughn, A.E. Hechanova, X. Yan, An experimental study of entrainment effects on the heat transfer from a flat surface to a heated circular impinging jet, J. Heat Transf. 113 (4) (1991) 1023–1025, http://dx.doi.org/10.1115/1.2911197.

[20] D. Lee, R. Greif, S.J. Lee, J.H. Lee, Heat transfer from a flat plate to a fully developed axisymmetric impinging jet, J. Heat Transf. 117 (3) (1995) 772–776, http://dx.doi.org/10.1115/1.2822647.

[21] J. Lee, S.-J. Lee, Stagnation region heat transfer of a turbulent axisymmetric jet impingement, Exp. Heat Transfer 12 (2) (1999) 137–156, http://dx.doi.org/10.1080/089161599269753.

[22] D.H. Lee, S.Y. Won, Y.T. Kim, Y. Suk Chung, Turbulent heat transfer from a flat surface to a swirling round impinging jet, Int. J. Heat Mass Transfer 45 (1) (2002) 223–227, http://dx.doi.org/10.1016/S0017-9310(01)00135-1.

[23] N. Gao, H. Sun, D. Ewing, Heat transfer to impinging round jets with triangular tabs, Int. J. Heat Mass Transfer 46 (14) (2003) 2557–2569, http://dx.doi.org/10.1016/S0017-9310(03)00034-6.

[24] M. Fenot, J.J. Vullierme, E. Dorignac, Local heat transfer due to several configurations of circular air jets impinging on a flat plate with and without semi-confinement, Int. J. Therm. Sci. 44 (7) (2005) 665–675, http://dx.doi.org/10.1016/j.ijthermalsci.2004.12.002.

[25] V. Katti, S.V. Prabhu, Experimental study and theoretical analysis of local heat transfer distribution between smooth flat surface and impinging air jet from a circular straight pipe nozzle, Int. J. Heat Mass Transfer 51 (17) (2008) 4480–4495, http://dx.doi.org/10.1016/j.ijheatmasstransfer.2007.12.024.

[26] R. Vinze, S. Chandel, M.D. Limaye, S.V. Prabhu, Influence of jet temperature and nozzle shape on the heat transfer distribution between a smooth plate and impinging air jets, Int. J. Therm. Sci. 99 (2016) 136–151, http://dx.doi.org/10.1016/j.ijthermalsci.2015.08.009.

[27] X.T. Trinh, M. Fénot, E. Dorignac, The effect of nozzle geometry on local convective heat transfer to unconfined impinging air jets, Exp. Therm. Fluid Sci. 70 (2016) 1–16, http://dx.doi.org/10.1016/j.expthermflusci.2015.08.006.

[28] X. Du, Z. Yang, Z. Jin, C. Xia, D. Bao, A comparative study of passive control on flow structure evolution and convective heat transfer enhancement for impinging jet, Int. J. Heat Mass Transfer 126 (2018) 256–280, http://dx.doi.org/10.1016/j.ijheatmasstransfer.2018.01.061.

[29] K. Yogi, M.M. Godase, M. Shetty, S. Krishnan, S.V. Prabhu, Experimental investigation on the local heat transfer with a circular jet impinging on a metal foamed flat plate, Int. J. Heat Mass Transfer 162 (2020) 120405, http://dx.doi.org/10.1016/j.ijheatmasstransfer.2020.120405.

[30] L.A. Gabour, J.H. Lienhard, Wall roughness effects on stagnation-point heat transfer beneath an impinging liquid jet, J. Heat Transf. 116 (1) (1994) 81–87, http://dx.doi.org/10.1115/1.2910887.

[31] A.H. Beitelmal, M.A. Saad, C.D. Patel, Effects of surface roughness on the average heat transfer of an impinging air jet, Int. Commun. Heat Mass Transfer 27 (1) (2000) 1–12, http://dx.doi.org/10.1016/S0735-1933(00)00079-8.

[32] N. Celik, Effects of the surface roughness on heat transfer of perpendicularly impinging co-axial jet, Heat Mass Transf. 47 (10) (2011) 1209–1217, http://dx.doi.org/10.1007/s00231-011-0785-9.

[33] W. Abu Rowin, Y. Xia, S. Wang, N. Hutchins, Accurately predicting turbulent heat transfer over rough walls: A review of measurement equipment and methods, Exp. Fluids 65 (6) (2024) 86, http://dx.doi.org/10.1007/s00348-024-03812-1.

[34] M. Bopp, T. Häber, F. Secchi, S. Schulz, S. Wegt, L. Krüger, R. Suntz, D. Trimis, B. Frohnapfel, S. Jakirlić, Mean flow and turbulence anisotropy representation in a round jet impingement: Experiment, DNS and modeling, 2025, submitted for publication.

[35] E. Napoli, V. Armenio, M. De Marchis, The effect of the slope of irregularly distributed roughness elements on turbulent wall-bounded flows, J. Fluid Mech. 613 (2008) 385–394, http://dx.doi.org/10.1017/S0022112008003571.

[36] F. Pèrez-Ràfols, A. Almqvist, Generating randomly rough surfaces with given height probability distribution and power spectrum, Tribol. Int. 131 (2019) 591–604, http://dx.doi.org/10.1016/j.triboint.2018.11.020.

[37] P. Forooghi, A. Weidenlener, F. Magagnato, B. Böhm, H. Kubach, T. Koch, B. Frohnapfel, DNS of momentum and heat transfer over rough surfaces based on realistic combustion chamber deposit geometries, Int. J. Heat Fluid Flow (ISSN: 0142-727X) 69 (2018) 83–94, http://dx.doi.org/10.1016/j.ijheatfluidflow.2017.12.002.

[38] G. Carlomagno, L. De Luca, G. Cardone, T. Astarita, Heat flux sensors for infrared thermography in convective heat transfer, Sensors 14 (11) (2014) 21065–21116, http://dx.doi.org/10.3390/s141121065.

[39] T. Astarita, G. Cardone, G.M. Carlomagno, Infrared thermography: An optical method in heat transfer and fluid flow visualisation, Opt. Lasers Eng. 44 (3) (2006) 261–281, http://dx.doi.org/10.1016/j.optlaseng.2005.04.006.

[40] A. Sielaff, Experimental Investigation of Single Bubbles and Bubble Interactions in Nucleate Boiling (Ph.D. thesis), Technische Universität, Darmstadt, 2014.

[41] K. Schweikert, A. Sielaff, P. Stephan, Pixel-wise in situ calibration method for high accuracy infrared thermography of moving targets, Infrared Phys. Technol. 118 (2021) 103862, http://dx.doi.org/10.1016/j.infrared.2021.103862.

[42] R. Hartley, A. Zisserman, Multiple View Geometry in Computer Vision, second ed., Cambridge University Press, Cambridge, 2004, http://dx.doi.org/10.1017/CBO9780511811685.

[43] S. van der Walt, J.L. Schönberger, J. Nunez-Iglesias, F. Boulogne, J.D. Warner, N. Yager, E. Gouillart, T. Yu, Scikit-image: Image processing in python, PeerJ 2 (2014) e453, http://dx.doi.org/10.7717/peerj.453.

[44] T.S. O'Donovan, D.B. Murray, Jet impingement heat transfer – Part I: Mean and root-mean-square heat transfer and velocity distributions, Int. J. Heat Mass Transfer 50 (17) (2007) 3291–3301, http://dx.doi.org/10.1016/j.ijheatmasstransfer.2007.01.044.

[45] T.S. O'Donovan, D.B. Murray, Jet impingement heat transfer – Part II: A temporal investigation of heat transfer and local fluid velocities, Int. J. Heat Mass Transfer 50 (17) (2007) 3302–3314, http://dx.doi.org/10.1016/j.ijheatmasstransfer.2007.01.047.

[46] T. Astarita, G.M. Carlomagno, Infrared Thermography for Thermo-Fluid-Dynamics, Springer, Berlin, Heidelberg, 2013, http://dx.doi.org/10.1007/978-3-642-29508-9.

[47] G.M. Carlomagno, G. Cardone, Infrared thermography for convective heat transfer measurements, Exp. Fluids 49 (6) (2010) 1187–1218, http://dx.doi.org/10.1007/s00348-010-0912-2.

[48] P.H. Broberg, E. Lindgaard, A.M. Olesen, S.M. Jensen, N.K.K. Stagsted, R.L. Bjerg, R. Grosselle, I.U. Oca, B.L.V. Bak, HISAPS: High-order smoothing spline with automatic parameter selection and shape constraints, SoftwareX 29 (2025) 102049, http://dx.doi.org/10.1016/j.softx.2025.102049.

[49] F. Secchi, Passive-Scalar Transfer in Complex Turbulent Flows (Ph.D. thesis), Karlsruher Institut für Technologie (KIT), 2025, http://dx.doi.org/10.5445/IR/1000185966.

[50] S. Roux, M. Fénot, G. Lalizel, L.-E. Brizzi, E. Dorignac, Experimental investigation of the flow and heat transfer of an impinging jet under acoustic excitation, Int. J. Heat Mass Transfer 54 (15) (2011) 3277–3290, http://dx.doi.org/10.1016/j.ijheatmasstransfer.2011.03.059.

[51] F. Secchi, D. Gatti, B. Frohnapfel, Heat transfer of an impinging jet - sensitivity towards inflow conditions, in: International ERCOFTAC Symposium on Engineering Turbulence Modelling and Measurements, Barcelona, 2023, http://dx.doi.org/10.5445/IR/1000170065.

[52] R. Viskanta, Heat transfer to impinging isothermal gas and flame jets, Exp. Therm. Fluid Sci 6 (2) (1993) 111–134, http://dx.doi.org/10.1016/0894-1777(93)90022-B.

[53] K. Jambunathan, E. Lai, M.A. Moss, B.L. Button, A review of heat transfer data for single circular jet impingement, Int. J. Heat Fluid Flow 13 (2) (1992) 106–115, http://dx.doi.org/10.1016/0142-727X(92)90017-4.

[54] M. Sibulkin, Heat transfer near the forward stagnation point of the body of revolution, J. Aeronaut. Sci. 19 (8) (1952) 570–571, http://dx.doi.org/10.2514/8.2383.

[55] D. Lytle, B. Webb, Air jet impingement heat transfer at low nozzle-plate spacings, Int. J. Heat Mass Transfer 37 (12) (1994) 1687–1697, http://dx.doi.org/10.1016/0017-9310(94)90059-0.

[56] V.V. Katti, S.N. Yasaswy, S.V. Prabhu, Local heat transfer distribution between smooth flat surface and impinging air jet from a circular nozzle at low Reynolds numbers, Heat Mass Transf. 47 (3) (2011) 237–244, http://dx.doi.org/10.1007/s00231-010-0716-1.

[57] M. Kadivar, D. Tormey, G. McGranaghan, A review on turbulent flow over rough surfaces: Fundamentals and theories, Int. J. Thermofluids 10 (2021) 100077, http://dx.doi.org/10.1016/j.ijft.2021.100077.